NRC·CNRC

NRC Publications Archive
Archives des publications du CNRC

Density functional theory and 3D-RISM-KH molecular theory of solvation studies of CO_2 reduction on Cu-, Cu_2O-, Fe-, and Fe_3O_4-based nanocatalysts

Kovalenko, Andriy; Neburchilov, Vladimir

This publication could be one of several versions: author's original, accepted manuscript or the publisher's version. / La version de cette publication peut être l'une des suivantes : la version prépublication de l'auteur, la version acceptée du manuscrit ou la version de l'éditeur.
For the publisher's version, please access the DOI link below./ Pour consulter la version de l'éditeur, utilisez le lien DOI ci-dessous.

Publisher's version / Version de l'éditeur:
https://doi.org/10.1007/s00894-020-04529-8
Journal of Molecular Modeling, 26, 10, pp. 1-10, 2020-09-12

NRC Publications Archive Record / Notice des Archives des publications du CNRC :
https://nrc-publications.canada.ca/eng/view/object/?id=4e49b372-aac4-40e9-a37a-ff7dae0b6b8d
https://publications-cnrc.canada.ca/fra/voir/objet/?id=4e49b372-aac4-40e9-a37a-ff7dae0b6b8d

Access and use of this website and the material on it are subject to the Terms and Conditions set forth at
https://nrc-publications.canada.ca/eng/copyright
READ THESE TERMS AND CONDITIONS CAREFULLY BEFORE USING THIS WEBSITE.

L'accès à ce site Web et l'utilisation de son contenu sont assujettis aux conditions présentées dans le site
https://publications-cnrc.canada.ca/fra/droits
LISEZ CES CONDITIONS ATTENTIVEMENT AVANT D'UTILISER CE SITE WEB.

Questions? Contact the NRC Publications Archive team at PublicationsArchive-ArchivesPublications@nrc-cnrc.gc.ca. If you wish to email the authors directly, please see the first page of the publication for their contact information.

Vous avez des questions? Nous pouvons vous aider. Pour communiquer directement avec un auteur, consultez la première page de la revue dans laquelle son article a été publié afin de trouver ses coordonnées. Si vous n'arrivez pas à les repérer, communiquez avec nous à PublicationsArchive-ArchivesPublications@nrc-cnrc.gc.ca.

National Research Council Canada | Conseil national de recherches Canada

Canada

Density Functional Theory and 3D-RISM-KH Molecular Theory of Solvation Studies of CO_2 Reduction on Cu, Cu_2O, Fe, and Fe_3O_4 Based Nanocatalysts

Andriy Kovalenko[1,2] and Vladimir Neburchilov[3]

[1] Nanotechnology Research Centre, National Research Council of Canada
11421 Saskatchewan Drive, Edmonton, Alberta, T6G 2M9, Canada. E-mail: andriy.kovalenko@nrc-cnrc-gc.ca
[2] Department of Mechanical Engineering, University of Alberta, Canada
10-203 Donadeo Innovation Centre for Engineering, 9211-116 Str., Edmonton, Alberta, T6G 1H9, Canada
E-mail: andriy.kovalenko@ualberta.ca
[3] Energy, Mining & Environment, Institute for Fuel Cell Innovation, National Research Council of Canada

Abstract: Using OpenMX quantum chemistry software for self-consistent field calculations of electronic structure with geometry optimization and 3D-RISM-KH molecular theory of solvation for 3D site distributions functions and solvation free energy, we modeled reduction of CO_2 + H_2 in ambient aqueous electrolyte solution of 1.0 Mol KH_2PO_4 into: (i) formic acid HCOOH, and (ii) CO + H_2O on the surfaces of Cu, Fe, Cu_2O, and Fe_3O_4 based nanocatalysts. It is applicable to its further reduction to hydrocarbons. The optimized geometries and free energies were obtained for the pathways of adsorption of the reactants from the solution, successive reduction on the surfaces of the nanocatalysts, and then release back to the solution bulk.

Keywords: CO_2 reduction to HCOOH; Cu, Cu_2O, Fe, Fe_3O_4 nanocatalysts; KH_2PO_4 ambient aqueous solution; OpenMX quantum chemistry; 3D-RISM-KH molecular theory of solvation

Introduction

Electrochemical reduction of CO_2 ($ECRCO_2$) to hydrocarbon fuels and chemicals is one of the promising clean-tech technologies. However, this new generation technology has one critical technical gap in terms of the insufficient stability and selectivity of the existing electrodes [1-3]. The main challenge in the development of efficient catalysts for $ECRCO_2$ is the significant list of factors effecting on their performance, including morphology, temperature, pressure, pH, type and concentration of electrolytes, type of solvent and membranes, electrolyte flow, and type of electrode (flat, porous, gas diffusion) [3]. By today, only two most efficient processes of ECRCO2 to carbon monooxide CO (CMO) and formic acid (FA) with a Faradaic efficiency (FA) of more than 90% at current density >100mA/cm^2 were developed [4]. The most developed catalysts for $ECRCO_2$ to formic acid are Cu- and Cu_2O-based catalysts.The first copper catalysts for $ECRCO_2$ to methane and ethylene were developed by Hori, with demonstrating beneficial performance in terms of the higher Faradaic efficiency compared to other catalysts [5]. Formic acid is another product of $ECRCO_2$ on Cu coming out through the formation of the intermediate formate [6]. This mechanism differs from the mechanism of $ECRCO_2$ to hydrocarbon fuels through the formation of the intermediate carbon [7,8]. The nanoparticle Cu electrocatalysts in contrast to polycrystylline Cu for $ECRCO_2$ improve the onset potential for both the products formic acid and CO through their oxidation and formation of oxide-derived copper (OD-Cu or Cu_2O). DFT proposes the formation of the intermediate COOH* through proton-electron transfer toward CO_2 radical interaction with two protons and one electron [9]. Carbon monoxide is another intermediate of $ECRCO_2$ toward C_2 hydrocarbons (-0.4 to -0.5V RHE) [10] among other 16 different products of this reaction on Cu/Cu_2O electrocatalysts. $ECRCO_2$ to C_2 hydrocarbons and probably to formic acid is more beneficial on Cu_2O-based catalysts compared to conventional Cu electrodes for the following reasons:

- Cu_2O has a higher surface roughness that allows to increase current density, consumption of protons, local pH, selectivity, current density [10],
- Cu_2O has a grain boundary and undercoordinated Cu atoms [11],
- Cu+ in Cu_2O is stabilized by the electrolyte and atomic rearrangement to undercoordinated Cu [10],
- Thinner catalyst layer and optimal preoxidation state and morphology [12].

The evaluation of catalyst Fe_3O_4 for $ECRCO_2$ shows that its selectivity to formic acid formation is less than that for Cu_2O-based catalyst. The DFT study of this process on a model electrode α-Fe_2O_3(0001) showed that methanol is the main product, with an overpotential η of 0.8 V over carbon monoxide (CO), formic acid (HCOOH), and formaldehyde (CH_2O) [13]. The mechanism of ECRCO2 to CO on Fe_3O_4 includes several kinetic stages, geometric contraction model $Fe_2O_3 \rightarrow Fe_3O_4$, $Fe_3O_4 \rightarrow FeO$ and $FeO \rightarrow Fe$ through nucleation and nuclei growth and diffusion. The activation energy of these three steps, including $Fe_2O_3 \rightarrow Fe_3O_4$, $Fe_3O_4 \rightarrow FeO$, and $FeO \rightarrow Fe$, is estimated to be 34.92 ± 1.24, 70.13 ± 0.88 and 44.12 ± 1.44 kJ/mol, respectively. The reduction of iron-based oxygen determines the efficiency of chemical looping hydrogen generation [14].

Theoretical modeling

A possible pathway of CO_2 and H_2 reduction into hydrocarbons under study here is its successive transformation into formate, then formic acid, and then CO and H_2O [15,16*]:

$$CO_2+H_2 \rightarrow CO_2*+2H* \rightarrow HCOO*+H* \rightarrow HCOOH* \rightarrow CO*+H_2O* \rightarrow CO+H_2O \quad (1)$$

It was studied on a set of catalysts – Ag, Au, Cu, Zn, Pt, Ni [17–19] – and lately on Sn catalyst [15]. From a combination of the insights gained from the *COOH and *OCHO volcanoes, a mechanism for CO_2RR to $2e^-$ products on Sn catalyst was presented [15].

Here we consider the process of transformation (1) on other nanocatalysts, nanocrystalline based Cu, Fe, Cu_2O, and Fe_3O_4 composites. The calculations were first carried out with the QM package OpenMX Ver. 3.9 [20]. The procedure then followed up with calculation of solvation structure and solvation free energy of these systems using the Three-Dimensional Reference Interaction Site Model with the Kovalenko-Hirata closure approximation (3D-RISM-KH) [21–23]. For the CO_2, H_2, H, HCOO, HCOOH, CO, H_2O molecules and for Cu, Fe, Cu_2O, Fe_3O_4 nanocatalysts, the 3D-RISM-KH calculations used the Universal Force Field (UFF) classical interaction potentials [24] and the partial charges and geometries obtained from running the OpenMX software package. The geometries for the species of ambient KH_2PO_4 aqueous solution were taken from UFF [24] and the partial charges of the species from AmberTools [25].

In the self-consistent field (SCF) calculations with OpenMX ver. 3.9 software [20], the following settings were used. The DFT calculations were performed using the Perdew-Burke-Ernzerhof (PBE) version [26] of the generalized gradient approximation (GGA) to the exchange-correlation potential. The levels of the approximation used for H, C, O atoms were H_PBE19, C_PBE19, O_PBE19, and for Cu atoms were Cu_PBE19H with the higher number of 19 valence electrons. The orbitals included in the calculation were at the so-called precise level of s2p2d1 for H, s3p2d2 for C and O, and s3p2d2f1 for Cu. The electronic temperature was set to 300.0 K. The energy cutoff was set to 120.0 Ry. The maximal number of iterations was set to 100. The supercell size

was set to 20Å×20Å×20Å. The SCF K-grid was chosen as 10×10×10. The SCF criterion was set equal to 1.0×10^{-10} Hartree.

Statistical mechanics based, 3D-RISM-KH molecular theory of solvation has proven to be an essential part of multiscale modeling framework covering a vast region of molecular simulation techniques. Successful applications range from solvation energy, structure, and phase behavior of small molecules to polymers, macromolecules, and biomolecules. 3D-RISM-KH successfully predicts and explains molecular mechanisms of self-assembly and conformational stability of synthetic organic rosette nanotubes, aggregation of proteins/peptides related to neurodegeneration, protein-ligand binding, and function-related solvation properties of biomolecules [21–23]]]]. The physics based RISM of molecular liquids describes a solvent molecule by a six-dimensional vector comprised of three positional $\{\mathbf{r}\}$ and three orientational $\{\Theta\}$ degrees of freedoms in the molecular Ornstein–Zernike equation via the total correlation function $h_\gamma(\mathbf{r})$ of interaction site γ of liquid at molecule position $\mathbf{r}$ and orientation Θ in 3D [27–29]. From a physical perspective, solvent is defined as a molecule with a finite number of site γ around a solute molecule of arbitrary shape, and the 3D site total correlation function $h_\gamma(\mathbf{r})$ is defined in terms of the 3D site direct correlation function $c_\gamma(\mathbf{r})$ as:

$$h_\gamma(\mathbf{r}) = \sum_\alpha \int d\mathbf{r}'\, c_\alpha(\mathbf{r}-\mathbf{r}')\, \chi_{\alpha\gamma}(r') \tag{1}$$

The 3D site distribution function of solvent molecules around the solute is calculated as $g_\gamma(\mathbf{r}) = h_\gamma(\mathbf{r}) + 1$. For a given temperature, the RISM formalism incorporates all sorts of interactions for all solvent sites. This construct is extremely helpful to build a solvent system containing multiple chemically distinct species, provided some characteristics of such mixed systems (e.g., density, dielectric constant, etc.) are known. An absolute requirement for solving equation (1) is to apply a closure relation. A closure is a mathematical formulation needed to connect the 3D total and direct correlation functions, and provides a computational handle to integrate the infinite chain of diagrams produced via equation (1). While several closure relations were developed over time, the Kovalenko-Hirata (KH) closure relation is shown to be numerically stable and providing solvation structures with reasonable accuracy. The KH closure approximation accounts for both electrostatic and non-polar features of any liquid(s), and has the following functional form:

$$g_\gamma(r) = \begin{cases} \exp\left(-u_\gamma(r)/(k_BT) + h_\gamma(r) - c_\gamma(r)\right) & \text{for} \quad g_\gamma(r) \le 1 \\ 1 - u_\gamma(r)/(k_BT) + h_\gamma(r) - c_\gamma(r) & \text{for} \quad g_\gamma(r) > 1 \end{cases} \tag{2}$$

The KH closure combines the so-called mean spherical approximation (applied to the spatial part with solvent density enrichment, $g_\gamma(\mathrm{r}) > 1$) with the hypernetted chain (HNC, applied to the spatial part with solvent density depletion, $g_\gamma(\mathrm{r}) < 1$) in a non-trivial way, thus providing numerical stability and accuracy. Computational cost for solving the 3D-RISM-KH equations is reasonable. The 3D-RISM-KH integral equations have an exact differential of the solvation free energy. This enables an analytical expression of Kirkwood's thermodynamic integration by gradually switching on the solute-solvent interaction:

$$\mu_{\mathrm{solv}} = \sum_\gamma \int d\mathbf{r}' \left(\frac{1}{2}h_\gamma^2(\mathbf{r})\theta(-h_\gamma(\mathbf{r})) - \frac{1}{2}h_\gamma(\mathbf{r})c_\gamma(\mathbf{r}) - c_\gamma(\mathbf{r})\right) \tag{1}$$

A well know drawback of the KH closure is that it underestimates the height of strong associative peaks. However, errors arising from that are mitigated by broadening of the peak, and often the

solvation thermodynamics and structure come out correctly. A detailed description of the 3D-RISM-KH theory was reported elsewhere [21–23].

Results

Figure 1 shows four catalyst supercells consisting of a single plate: (i) face-centered cubic (FCC) arrangement of 21 Cu atoms (lattice constant 3.6149 Å) and with a 2-atom vacancy at the supercell top, (ii) body-centered (BCC) arrangement of 28 Fe atoms (lattice constant 2.8665 Å) and with a 2-atom vacancy at the supercell top, (iii) arrangement of 72 Cu and 36 O atoms (lattice constant 4.2910 Å), and (iv) arrangement of 54 Fe and 72 O atoms (lattice constant 8.53335 Å). In the simulations, the catalyst structure was fixed, while the molecules of adsorbates (H_2, H, CO2, HCOO, HCOOH, CO, H_2O) underwent self-consistent optimization of electronic and geometric structure.

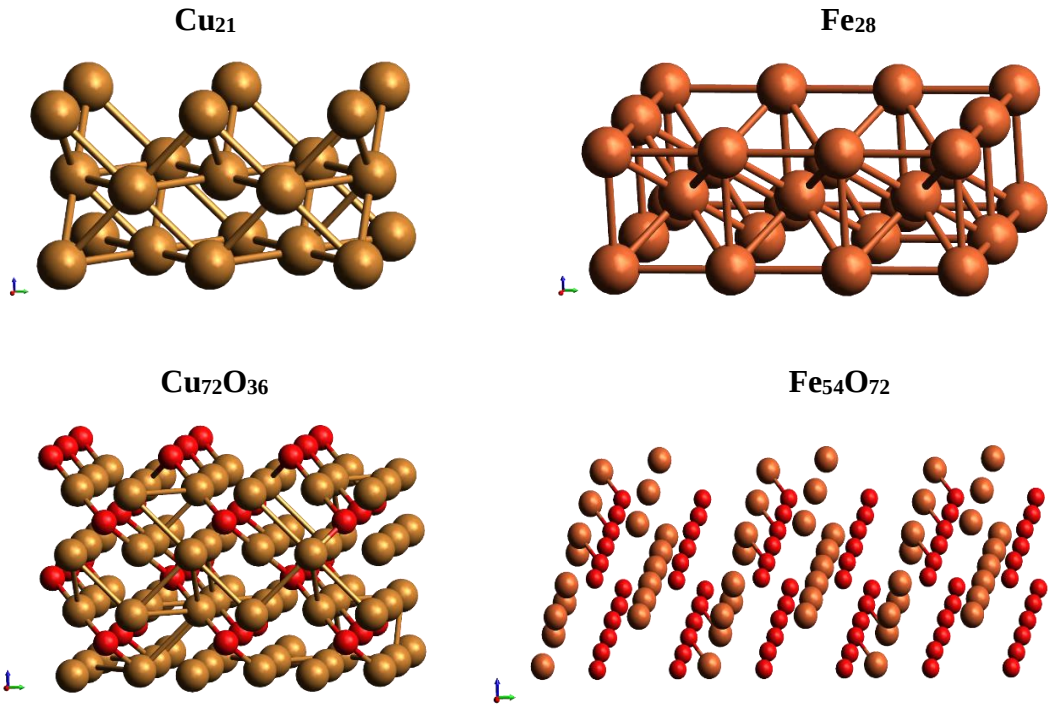

Figure 1. Structure of the nanocatalyst supercell: Cu_{21} atoms with a 2-atom vacancy on top; Fe_{28} atoms with a 2-atom vacancy on top; $Cu_{72}O_{36}$ atoms; $Fe_{54}O_{72}$ atoms.

The SCF calculations with OpenMX were first run for each of the supercell slab of 21 Cu, 28 Fe, 72 Cu – 36 O, and 54 Fe – 72 O atoms in 1.0 Mol KH_2PO_4 aqueous solution. Then the SCF calculations were run successively with H_2, H, CO_2, HCOO, HCOOH, CO, H_2O molecules at the surface of each of the four nanocatalysts slabs in the solution. Finally, the simulations were run for pure H_2, H, CO_2, HCOO, HCOOH, CO, H_2O molecules in the solution.

Figures 2 – 5 depict the arrangements of the H_2*, H*, CO_2*, HCOO*, HCOOH*, CO*, and H_2O* molecules adsorbed from 1.0 Mol KH_2PO_4 ambient aqueous solution at the surface of the Cu, Fe, Cu_2O, and Fe_3O_4 slab nanocatalysts, respectively.

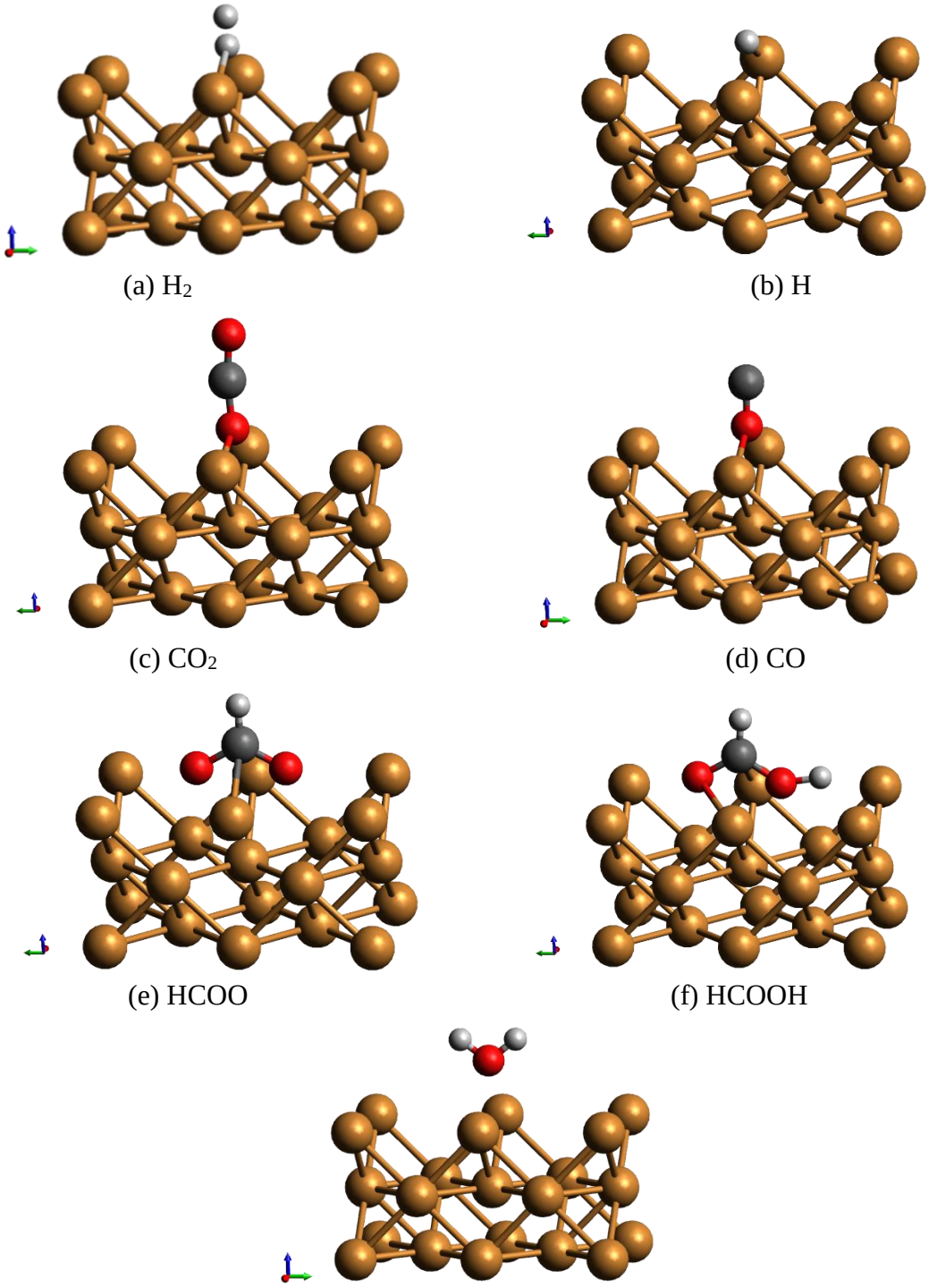

(a) H_2 (b) H

(c) CO_2 (d) CO

(e) HCOO (f) HCOOH

(g) H_2O

Figure 2. Positions of H_2*, H*, CO_2*, HCOO*, HCOOH*, CO*, and H_2O* molecules adsorbed over the 2-atom vacancy on top of the Cu_{21} slab nanocatalyst in ambient 1.0 Mol KH_2PO_4 aqueous solution.

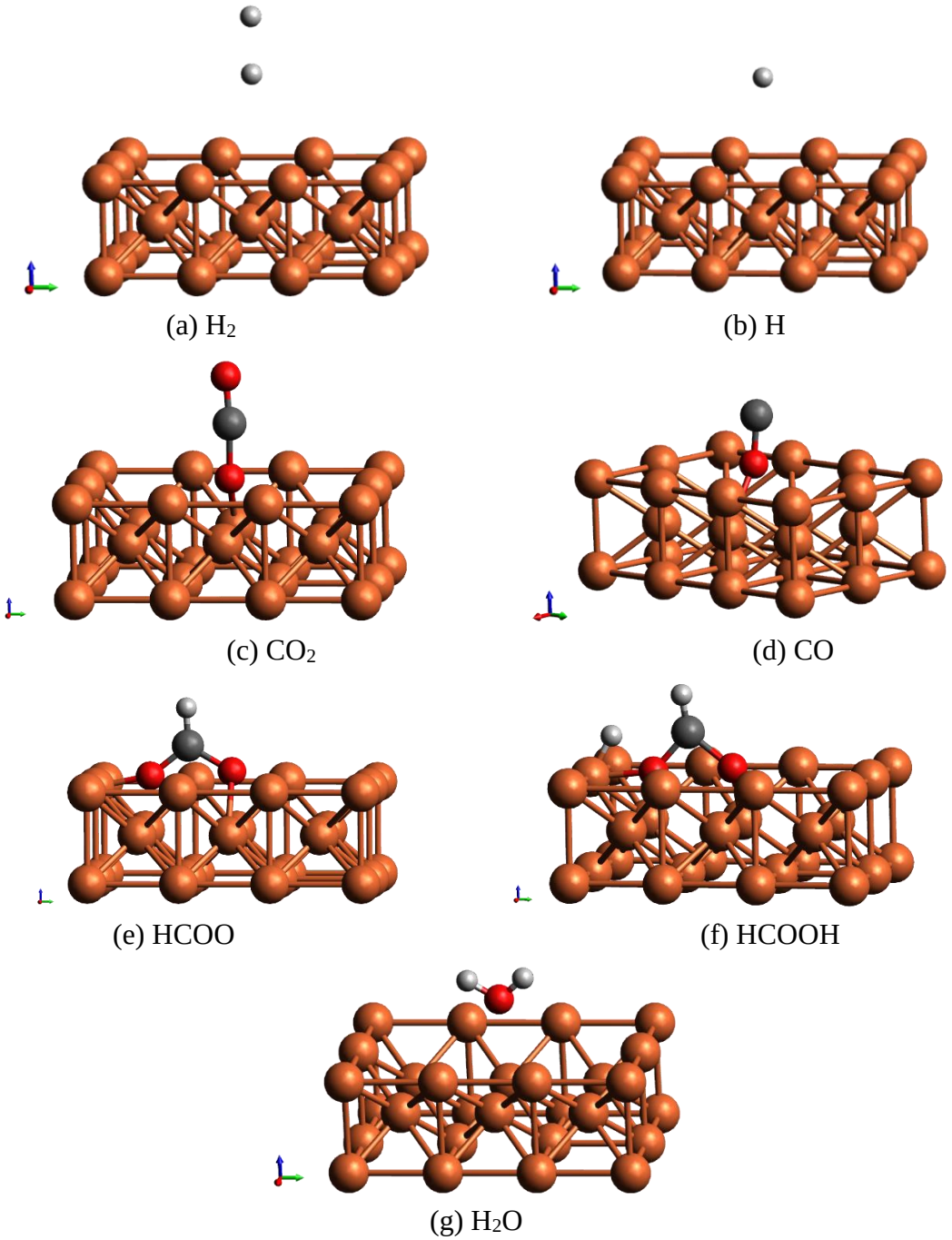

Figure 3. Same as in Figure 2 but for the 2-atom vacancy on top of the Fe_{28} slab nanocatalyst.

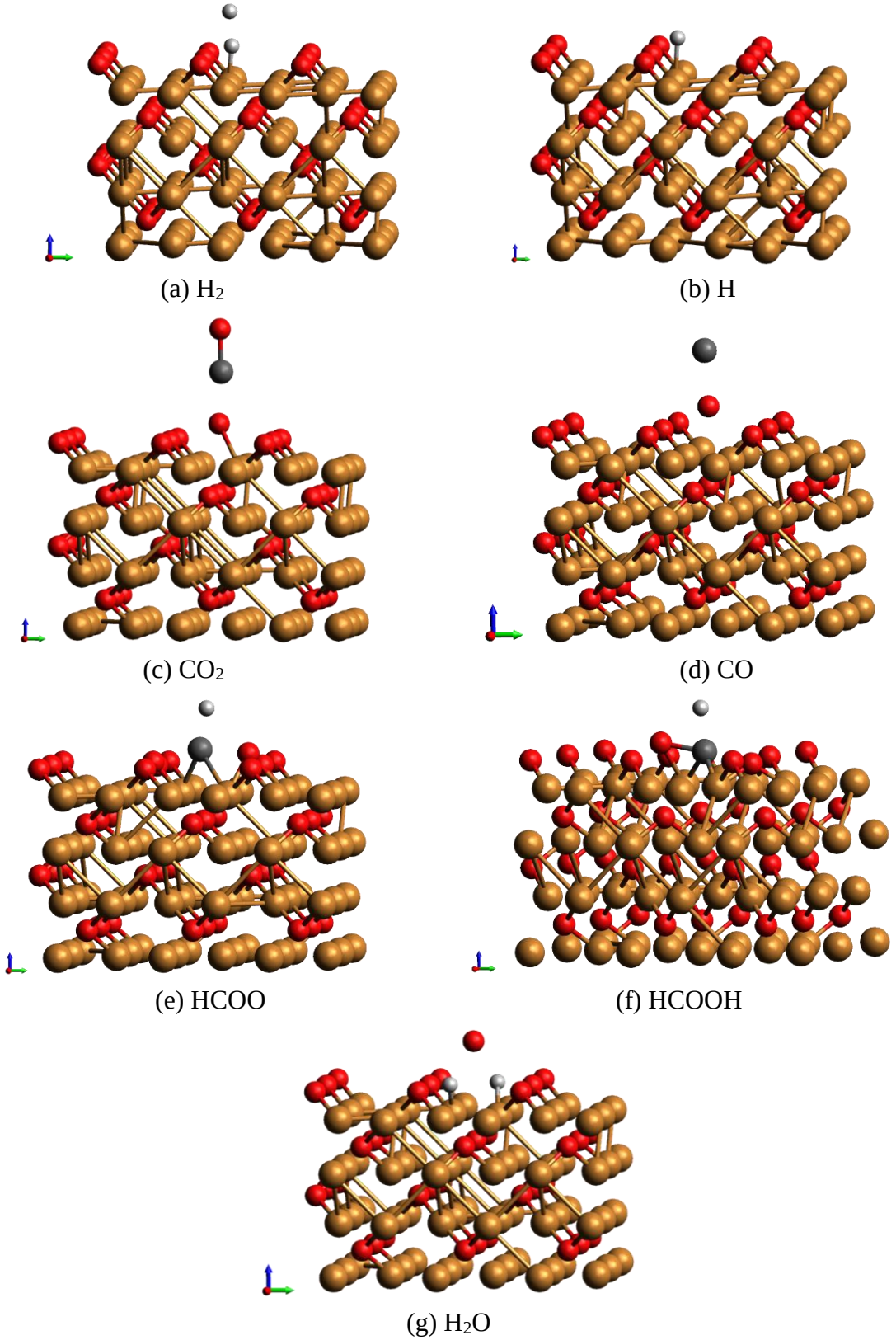

Figure 4. Positions of the H_2*, H*, CO_2*, HCOO*, HCOOH*, CO*, and H_2O* molecules adsorbed on top of the $Cu_{72}O_{36}$ slab nanocatalyst in ambient 1.0 Mol KH_2PO_4 aqueous solution.

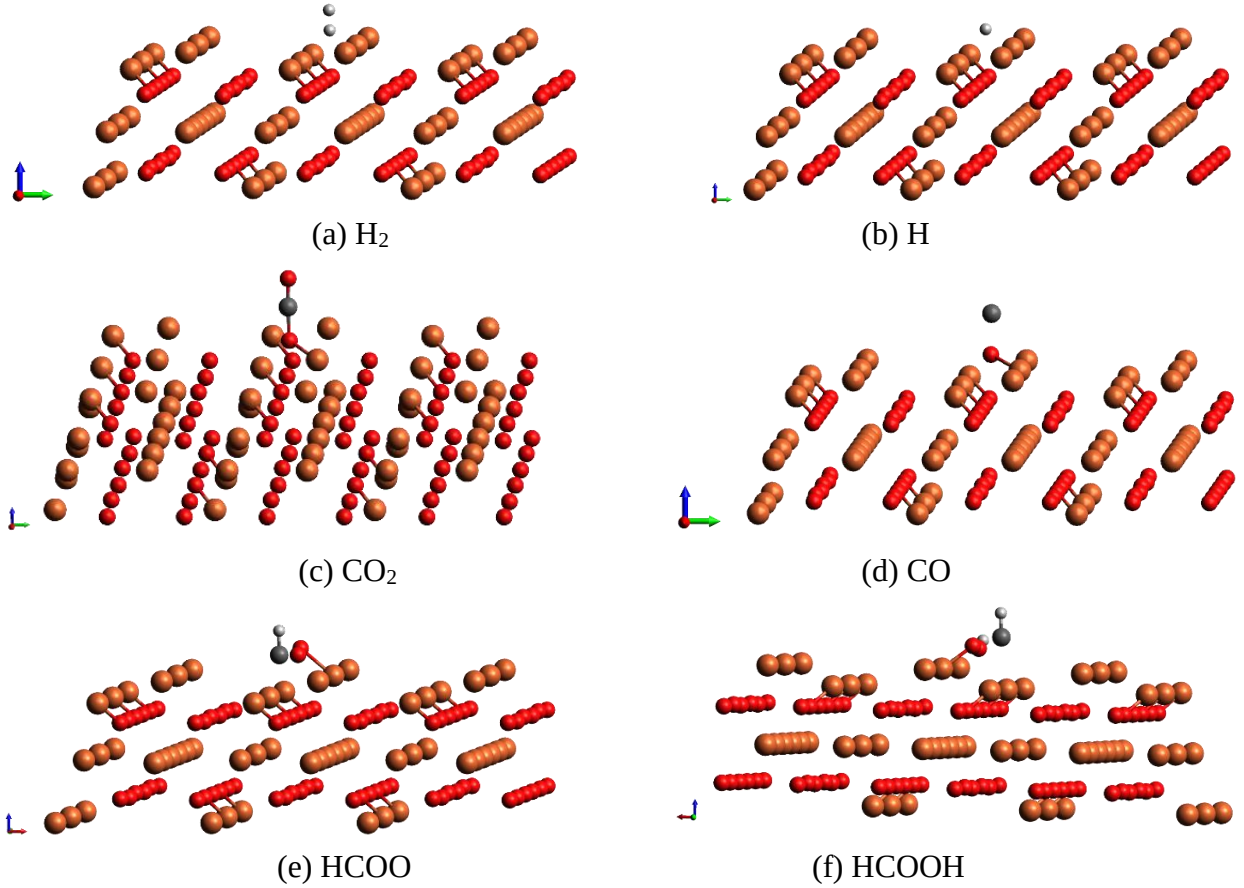

(a) H_2 (b) H

(c) CO_2 (d) CO

(e) HCOO (f) HCOOH

(g) H_2O

Figure 5. Same as in Figure 4 but for $Fe_{54}O_{72}$ atoms slab nanocatalyst.

Table 1 presents the free energies of the molecules reduction (1) in 1.0 Mol KH_2PO_4 ambient aqueous solution on the Cu_{21}, Fe_{28}, $Cu_{72}O_{36}$, and $Fe_{54}O_{72}$ nanocatalysts. Figures 6 to 9 show the free energies in the successive steps of adsorption and reduction of CO_2* and H_2* into CO_2*+2H,* formate HCOO*+H*, formic acid HCOOH*, and then CO*+H_2O* at the surface of the Cu_{21}, Fe_{28}, $Cu_{32}O_{72}$, and $Fe_{28}O_{72}$ slab nanocatalysts, respectively, in ambient aqueous electrolyte solution of 1.0 Mol KH_2PO_4, with final release of HCOOH and CO+H_2O back to the solution.

At the first step of adsorption of CO_2 and H_2, H_2* splitting into 2H*, and conversion into HCOO* on the Cu_{21} slab nanocatalyst, the free energy increase for CO_2 is almost entirely offset with the free energy decrease for H_2 (Table 1, Figure 6). The free energy then significantly decreases with conversion of HCOO* and another H* into HCOOH* adsorbed on the the Cu_{21} slab. The free energy decreases even more with release of HCOOH* from the Cu_{21} nanocatalyst into the 1.0 Mol KH_2PO_4 aqueous solution bulk. In a parallel route, the free energy increases with further conversion of HCOOH* into CO*+H_2O* on the Cu_{21} slab, and somewhat decreases with their release into the solution bulk.

On the Fe_{28} slab nanocatalyst, the free energy of H_2* first increases with adsorption and splitting into 2H*, whereas the free energy of CO_2* significantly increases with adsorption (Table 1, Figure 7). The free energy significantly decreases with conversion into HCOO* and then increases half way back with further conversion into HCOOH*. However, the overall free energy of the second stage of conversion of HCOO* and H* into HCOOH* decreases, and then further significantly decreases with release of HCOOH* to the solution bulk, bringing the free energy of the end product HCOO* of the conversion to be almost the same as that of the reactants CO_2*+H_2*. Further, in the parallel route, the free energy somewhat decreases with conversion of HCOO* into CO*+H_2O*, and then decreases even more with release of CO* and H_2O* into the solution bulk, bringing it to the value somewhat higher than for the initial reactants CO_2 and H_2.

The behavior of the free energy in adsorption and reduction of CO_2 and H_2 into CO_2*+2H*, formate HCOO*+H*, formic acid HCOOH*, and then CO*+H_2O* at the surface of both the $Cu_{32}O_{72}$ and $Fe_{28}O_{72}$ slab nanocatalysts in ambient aqueous electrolyte solution of 1.0 Mol KH_2PO_4 with final desorption of HCOOH* and CO*+H_2O* into the solution bulk is quite similar to the Cu_{21} slab nanocatalyst (Table 1, Figures 8 and 9).

Table 1. Free energies of CO_2*, H_2*, H*, HCOO*, HCOOH*, CO*, OH*, and H_2O* molecules in the process of reduction in 1.0 Mol KH_2PO_4 ambient aqueous solution from CO_2*+H_2* to CO*+H_2O* on the surface of the 2-vacancy Cu_{21}, 2-vacancy Fe_{28}, $Cu_{72}O_{36}$, and $Fe_{54}O_{72}$ nanocatalyst slabs.

Step	Free Energy (kcal/mol) of Nanocatalyst Slab			
	Cu_{21}	Fe_{28}	$Cu_{72}O_{36}$	$Fe_{54}O_{72}$
CO_2 in bulk	-213.25919			
H_2 in bulk	7.05012			
CO_2*	-202.52158	-32.61447	-157.76562	-181.19848
H_2*	5.45143	-78.45407	3.81933	3.33911
H*	3.81116	65.28411	6.04975	5.50439
HCOO*	-165.89450	20.90473	-120.13377	-150.91931
HCOOH*	-203.80180	112.02679	-136.00195	-184.56921
CO*	-23.04370	216.76891	-27.01173	-17.77649
OH*	-20.70987	-61.70029	-15.44338	-21.52698
H_2O*	-107.53037	-116.32019	-55.06541	-87.14221
CO in bulk	-24.359351			
H_2O in bulk	-111.365682			

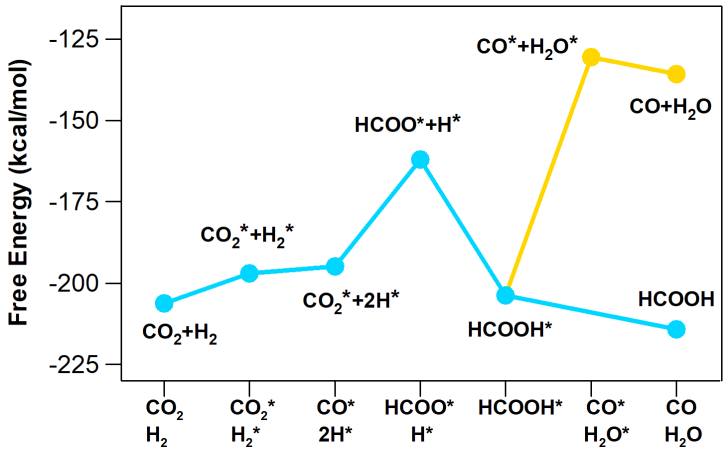

Figure 6. Free energies of successively reducing CO_2+H_2 from 1.0 Mol KH_2PO_4 ambient aqueous solution to CO_2*+2H*, formate HCOO*+H*, and then formic acid HCOOH* and CO*+H_2O* on the surface of the 2-vacancy Cu_{21} nanocatalyst slab, with final release back to the solution.

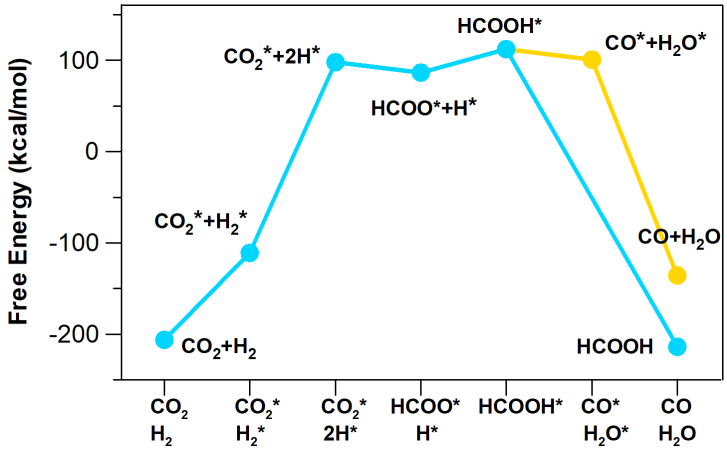

Figure 7. Same as in Figure 6 but for the 2-atom vacancy on top of the Fe_{28} slab nanocatalyst.

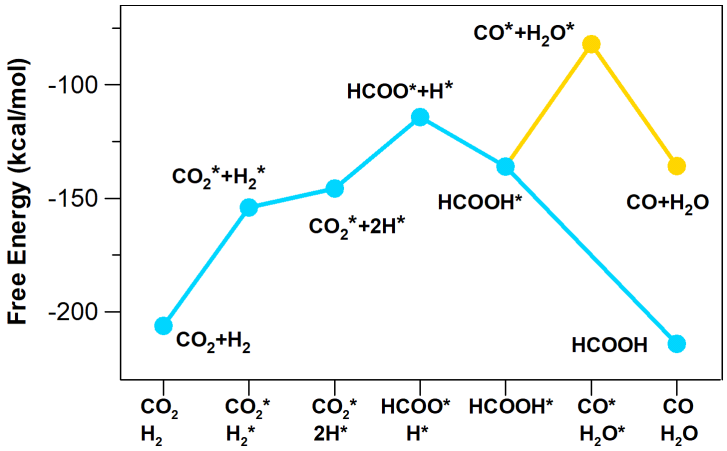

Figure 8. Free energies of successively reducing CO_2+H_2 from 1.0 Mol KH_2PO_4 ambient aqueous solution to CO_2*+2H*, formate HCOO*+H*, and then formic acid HCOOH* and CO*+H_2O* on the surface of the $Cu_{72}O_{36}$ nanocatalyst slab, with final release back to the solution.

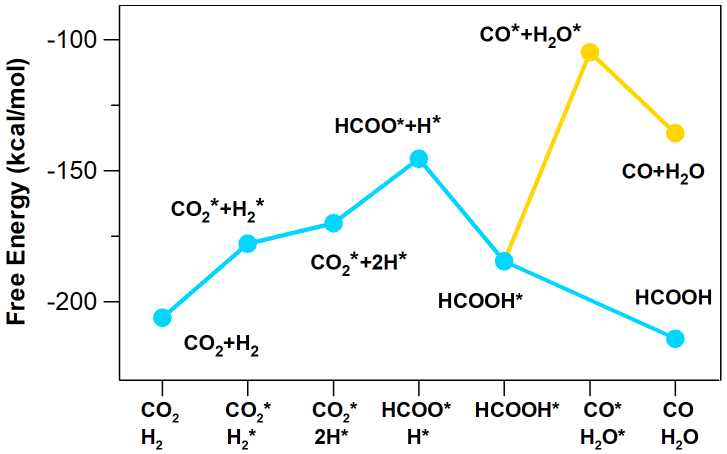

Figure 9. Same as in Figure 8 but for the $Fe_{54}O_{72}$ slab nanocatalyst.

To illustrate the effect of the KH_2PO_4 aqueous solution, Figures 10 to 13 show the free energies in the successive steps of adsorption and reduction of CO_2 and H_2 into CO_2*+2H*, formate HCOO*+H*, formic acid HCOOH*, and then CO*+H_2O* at the surface of the Cu_{21}, Fe_{28}, $Cu_{32}O_{72}$, and $Fe_{28}O_{72}$ slab nanocatalysts, respectively, but without solution. As before, the free energies were obtained using the SCF calculations with OpenMX software with geometry optimization, whereas the 3D-RISM-KH calculations of the 3D distribution functions and the solvation free energies in the solution were removed. The results are substantially different from the calculation including the effects of both the nanocatalysts and the KH_2PO_4 aqueous solution. All the barriers of free energy in the reduction pathway CO_2+H_2 → CO_2*+H_2* → CO_2*+2H* → HCOO*+H* → HCOOH* → CO*+H_2O* → CO+H_2O are significantly higher in the absence of the solution.

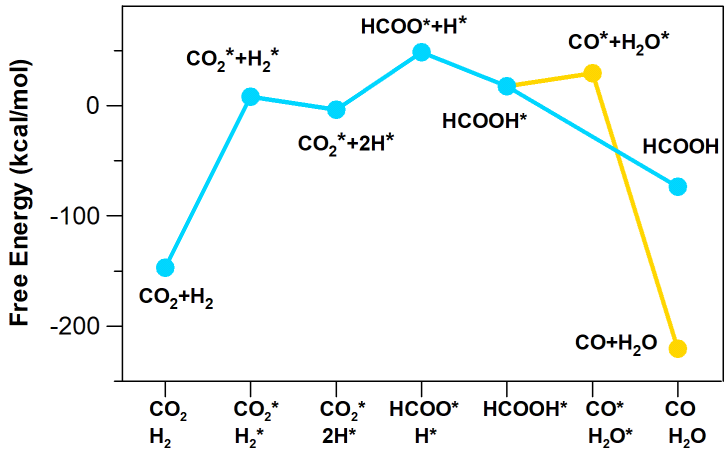

Figure 10. Free energies of successively reducing CO_2+H_2 from the bulk but without solution to CO_2*+2H*, formate HCOO*+H*, and then formic acid HCOOH* and CO*+H_2O* on the surface of the 2-vacancy Cu_{21} nanocatalyst slab, with final release back to the bulk.

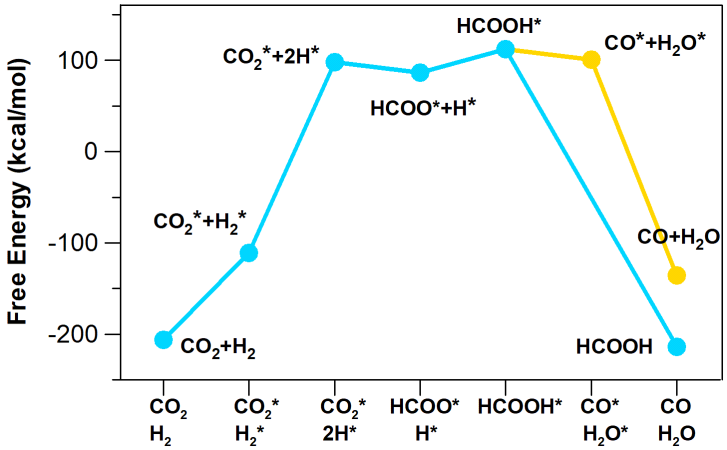

Figure 11. Same as in Figure 10 but for the 2-atom vacancy on top of the Fe_{28} slab nanocatalyst.

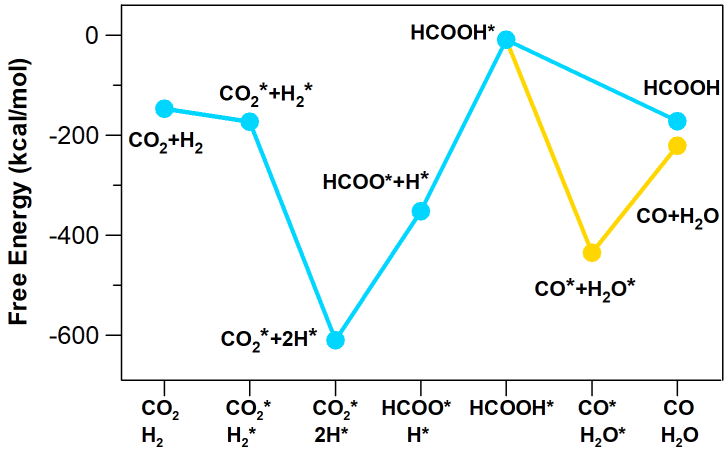

Figure 12. Free energies of successively reducing CO_2+H_2 from the bulk but without solution to CO_2*+2H*, formate HCOO*+H*, and then formic acid HCOOH* and CO*+H_2O* on the surface of the 2-vacancy $Cu_{72}O_{36}$ nanocatalyst slab, with final release back to the bulk.

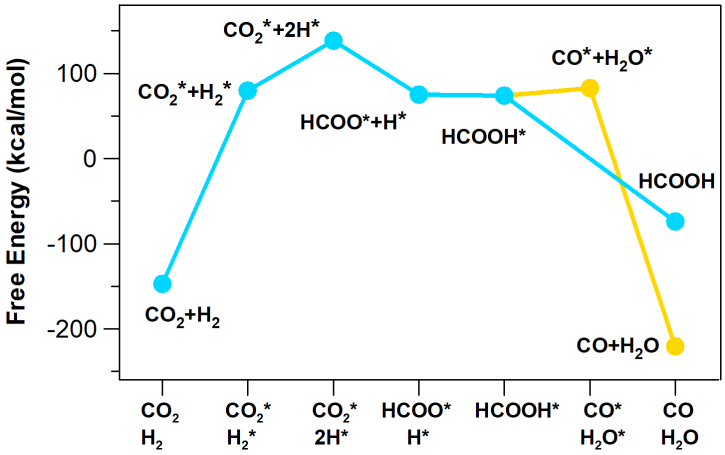

Figure 13. Same as in Figure 12 but for the $Fe_{54}O_{72}$ slab nanocatalyst.

Conclusion

We developed and tested a multiscale modeling description of CO_2 + H_2 reduction that couples: (i) OpenMX software for quantum chemical self-consistent field (SCF) calculations of electronic structure with geometry optimization, and (ii) 3D-RISM-KH molecular theory of solvation for 3D site distribution functions and solvation free energies of molecules at slab nanocatalysts in electrolyte solutions.

The description was applied to Cu_{21}, Fe28, $Cu_{72}O_{36}$, and $Fe_{54}O_{72}$ slab nanocatalyst in ambient aqueous electrolyte solution of 1.0 M KH_2PO_4 to predict successive steps of CO_2 + H_2 reduction along two competitive pathways:

1) $CO_2+H_2 \rightarrow CO_2*+2H* \rightarrow HCOO*+H* \rightarrow HCOOH* \rightarrow HCOOH$
2) $CO_2+H_2 \rightarrow CO_2*+2H* \rightarrow HCOO*+H* \rightarrow HCOOH* \rightarrow CO*+H_2O* \rightarrow CO+H_2O$

Our new SCF calculations with OpenMX coupled with 3D-RISM-KH theory for electrochemical reduction of CO_2 and H_2 to formate HCOO, formic acid HCOOH, and then further to CO and H_2O using Cu, Cu_2O, Fe, and Fe_3O_4-based nanocatalysts in ambient aqueous electrolyte solution of 1.0 M KH_2PO_4 showed a viability of these systems. All these nanocatalysts were predicted to provide a good yield (with free energy decrease) for the $CO_2+H_2 \rightarrow$ HCOOH reduction pathway. For the $CO_2+H_2 \rightarrow CO+H_2O$ reduction pathway, Fe nanocatalyst still provides good conversion with a little increase of the free energy, whereas the other three nanocatalysts perform with the free energy increase three to five times larger than that for Fe.

Recently, a predominant shape-dependent electrocatalytic reduction of CO_2 to CO on triangular silver nanoplates (Tri-Ag-NPs) in 0.1 M $KHCO_3$ aqueous electrolyte solution was studied [30]. It exhibited an enhanced current density and significantly improved Faradaic efficiency (96.8%) and energy efficiency (61.7%), together with a considerable durability (7 days). DFT calculations were explored to investigate the reactivity of different Ag features based on the computational hydrogen electrode model. Figure 13 shows the Gibbs free energy (ΔG) diagram for CO_2RR on different facets and Ag_{55} cluster, where the total ΔG values required for the proposed four elementary reaction steps were simulated and calculated [30]. The required overpotential η initially originates from the formation of HCOO* because an uphill energy barrier of the first proton-coupled electron transfer step for all facets and the cluster was observed. The free-energy step subsequently becomes more thermodynamically facile for the second proton-coupled electron transfer for the adsorbed CO* at all facets. The free-energy step subsequently becomes more thermodynamically facile for the second proton-coupled electron transfer for the adsorbed CO* at all facets. Although the Ag_{55} cluster is slightly easier for the formation of HCOO* than all facets, it tends to overbind with CO* and consequently decreases the product evolution rate. Thus, both the dominance of at the facet of Ag(100) and the ease in the CO evolution deriving from the shape controlled effect point to the decreased η and low onset potential for CO formation. These free energy diagrams for electrocatalytic reduction on Ag nanocatalyst in 0.1 M $KHCO_3$ aqueous electrolyte solution exhibited the behavior quite similar to our results for the reduction on Cu, Fe, Cu_2O, and Fe_3O_4 nanocatalysts in 1.0 M KH_2PO_4 aqueous solution (Figures 6 to 9).

There is a possibility of selecting a particular nanocatalyst to optimize the performance of these systems. Our future studies will extend this work further to involving the Fischer-Tropsch process for reduction of CO_2+H_2 to hydrocarbons.

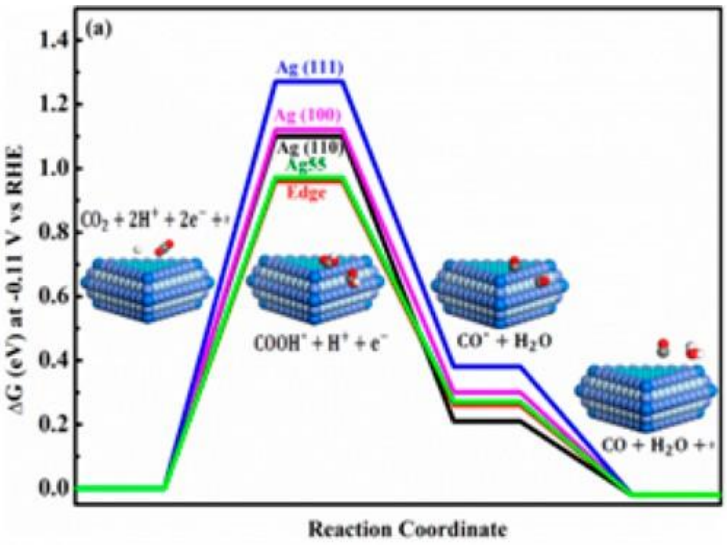

Figure 13. Free energy diagrams for CO_2RR to CO on different facets and Ag_{55} cluster at voltage −0.11 V [30]. Copyright 2017 American Chemical Society.

References

[1] Ross, M.B.; De Luna, P.; Li. Y.; Dinh, C.-T.; Kim, D.; Yang, P.; Sargent, E. H. *Nature catalysis* **2019**, *2*, 648−658.

[2] He, J.; Johnson, N.J.J.; Huang, A.; Berlinguette, C.P. *ChemSusChem* **2018**, *11*, 48−57.

[3] Zhou, H.; Liu, K.; Li, H.; Cao, M.; Fu, J.; Gao, X.; Hu, J.; Li, W.; Pan, H.; Zhan, J.; Li, Q.; Qiu, X.; Liu, M. *J. Coll. Interface Sci* **2019**, *550*, 17−47.

[4] Rahbari, A.; Ramdin, M.; van den Broeke, L.J.P.; Vlugt, T.J.H. *Ind. Eng. Chem. Res.* **2018**, *57*, 10663−10674.

[5] Yoshio, H.; Katsuhei, K.; Shin, S. *Chem. Lett*. **1985**, *11*, 1695−1698.

[6] Jitaru, M.; Lowy, D.A.; Toma, M.; Toma, B.C.; Oniciu, L. *J. Appl. Electrochem*, **1997**, *27*, 875−889.

[7] Hori, Y.; Murata, A.; Takahashi, R. *J. Chem. Soc. Farad. Trans. 1* **1989**, *85(8)*, 2309−2326.

[8] Hori, Y.; Takahashi, R.; Yoshinami, Y.; Murata, A. *J. Phys. Chem. B* **1997**, *101*, 7075−7081.

[9] Kortlever, R.; Shen, J.; Schouten, K.J.; Calle-Vallejo, F.; Koper, M.T. *J. Phys. Chem. Lett*. **2015**, *6(20)*, 4073−4082.

[10] Li, C.; Kanan, M.W. *J. Am. Chem. Soc*. **2012**, *134*, 7231−7234.

[11] Li, C.; Ciston, J.; Kanak, M.W. *Nature* **2014**, *508*, 504−507.

[12] Roberts, F.S.; Kuhl, K.P.; Nilsson, A. *Angew. Chem. Int. Ed*. **2015**, *54*, 5179−5182.

[13] Kumar, N.; Seriani, N.; Gebauer, R. *Phys. Chem. Chem. Phys*. **2020** (in press); DOI : 10.1039/C9CP06453B

[14] Wang, Y.D.; Hua, X.N.; Zhao, C.C.; Fu, T.T.; Li, W.; Wang, W. *Int. J. Hydrogen Energy* **2017**, *42(9)*, 5667−5675.

[15] Feaster, J. T.; Shi, C.; Cave, E. R.; Hatsukade, T.; Abram, D. N.; Kuhl, K. P.; Hahn, C.; Nørskov, J. K.; Jaramillo, T. F. *ACS Catal*. **2017**, *7*, 4822−4827.

[16] Choi, S.; Sang, B.-I.; Hong, J.; Yoon, K. J.; Son, J.-W.; Lee, J.-H.; Kim, B.-K.; Kim, H. *Sci. Rep.* **2017**, *7*, 41207–10.

[17] Kuhl, K. P.; Hatsukade, T.; Cave, E. R.; Abram, D. N.; Kibsgaard, J.; Jaramillo, T. F. *J. Am. Chem. Soc*. **2014**, *136*, 14107−14113.

[18] Kuhl, K. P.; Cave, E. R.; Abram, D. N.; Jaramillo, T. F. *Energy Environ. Sci.* **2012**, *5*, 7050−7059.

[19] Hatsukade, T.; Kuhl, K. P.; Cave, E. R.; Abram, D. N.; Jaramillo, T. F. *Phys. Chem. Chem. Phys.* **2014**, *16*, 13814−13819.

[20] Lejaeghere, K.; et al. *Science* **2016**, *351(6280)*, aad3000.

[21] Kovalenko, A. *Pure Appl. Chem.* **2013**, *85*, 159–199.

[22] Kovalenko, A. Multiscale modeling of solvation. In: *Springer Handbook of Electrochemistry*. Breitkopf, C.; Swider-Lyons, K. (Eds.) Springer Handbooks, pp. 95-139. Springer-Verlag Berlin Heidelberg, 2017, 1016 p.

[23] Kovalenko, A.; Gusarov, S. *Phys. Chem. Chem. Phys.* **2018**, *20*, 2947−2969.

[24] Rappe, A.K.; Casewit, C.J.; Colwell, K.S.; Goddard III, W.A.; Skiff, W.M. *J. Am. Chem. Soc.* **1992**, 1*14*, 10024-10035.

[25] Case, D.A.; Belfon, K.; Ben-Shalom, I.Y.; Brozell, S.R.; Cerutti, D.S.; Cheatham, III, T.E.; Cruzeiro, V.W.D.; Darden, T.A.; Duke, R.E.; Giambasu, G.; Gilson, M.K.; Gohlke, H.; Goetz, A.W.; Harris, R.; Izadi, S.; Kasava-jhala, K.; Kovalenko, A.; Krasny, R.; Kurtzman, T.; Lee, T.S.; LeGrand, S.; Li, P.; Lin, C.; Liu, J.; Luchko, T.; Luo, R.; Man, V.; Merz, K.M.; Miao, Y.; Mikhailovskii, O.; Monard, G.; Nguyen, H.; Onufriev, A.; Pan, F.; Pantano, S.; Qi, R.; Roe, D.R.; Roitberg, A.; Sagui, C.; Schott-Verdugo, S.; Shen, J.; Simmerling, C.L.; Skrynnikov, N.; Smith, J.; Swails, J.; Walker, R.C.; Wang, J.; Wilson, L.; Wolf, R.M.; Wu, X.; York, D.M.; Kollman, P.A. *AMBER 2020*, 2020, University of California, San Francisco. https://ambermd.org/

[26] Perdew, J. P.; Burke, K.; Ernzerhof, M. *Phys. Rev. Lett.* **1996**, *77*, 3865−3868.

[27] Chandler, D.; McCoy, J. D.; Singer, S. J. Density Functional Theory of Nonuniform Polyatomic Systems. I. General Formulation. *J. Chem. Phys.* **1986**, *85*, 5971–5976.

[28] Chandler, D.; McCoy, J. D.; Singer, S. J. Density Functional Theory of Nonuniform Polyatomic Systems. II. Rational Closures for Integral Equations. *J. Chem. Phys*. **1986**, *85*, 5977–5982.

[29] Hansen, J.-P.; McDonald, I. R. Theory of Simple Liquids, 3rd ed.; Elsevier Academic Press: London Burlington, **2006**.

[30] Liu, S.; Tao, H.; Zeng, L.; Liu, Q.; Xu, Z.; Liu, Q.; Luo, J.-L. *J. Am. Chem. Soc.* **2017**, *139*, 2160−2163.